CHEMICAL PHYSICS

On-surface synthesis of Heisenberg spin-1/2 antiferromagnetic molecular chains

Kewei Sun[1,2], Nan Cao[3], Orlando J. Silveira[3], Adolfo O. Fumega[3], Fiona Hanindita[4], Shingo Ito[4]*, Jose L. Lado[3], Peter Liljeroth[3], Adam S. Foster[3,5]*, Shigeki Kawai[2,6]*

Magnetic exchange interactions between localized spins in π-electron magnetism of carbon-based nanostructures have attracted tremendous interest due to their great potential for nano spintronics. Unique many-body quantum characteristics, such as gaped excitations, strong spin entanglement, and fractionalized excitations, have been demonstrated, but the spin-1/2 Heisenberg model with a single antiferromagnetic coupling J value remained unexplored. Here, we realized the entangled antiferromagnetic quantum spin-1/2 Heisenberg model with diazahexabenzocoronene oligomers (up to 7 units) on Au(111). Extensive low-temperature scanning tunneling microscopy/spectroscopy measurements and density functional theory and many-body calculations show that even-numbered spin chains host a collective state with gapped excitations, while odd-numbered chains feature a Kondo excitation. We found that a given antiferromagnetic coupling J value between first neighbors in the entangled quantum states is responsible for the quantum phenomena, strongly relating to their parities of the chain. The tunable molecular building blocks act as an ideal platform for the experimental realization of topological spin lattices.

INTRODUCTION

Atomically defined carbon nanostructures hosting π-electron magnetism (1) have great potential as nanoscale magnetic components in spin-electronic devices (2–4). Compared to d/f-electron magnetism in transition metal elements, π-electrons in the molecules are usually more delocalized, and the weak spin-orbit interaction with long spin coherence time and length (5–9) is expected to exhibit tunable quantum properties. A key development target is the fabrication of various atomically defined carbon nanostructures with spin polarization, offering a platform for investigating low-energy excitations. However, since molecules with unpaired electrons are usually highly reactive and short-lived, the synthesis is challenging by solution-based chemical reactions. On-surface synthesis has been developed to fabricate atomically accurate carbon-based nanostructures via activation and conjugation of precursor molecules on metal substrates (10, 11) and has opened an exciting possibility of studying low-energy spin excitations in carbon-based materials. Several nanographene structures and graphene nanoribbons with unpaired π-electrons or zigzag edges have been successfully synthesized and characterized on surfaces, and their magnetic properties give rise to a variety of correlated phases (12–24). For example, magnetic chains have been fabricated by conjugating triangulenes and porphyrin oligomers, and the Coulomb repulsion between the π-electrons in each unit that compose the chains gives rise to an antiferromagnetic ordering, bringing the whole chain to a topological Haldane spin chain phase (24–27). Another strategy to achieve different

correlated scenarios in a controlled manner is to consider nitrogen doping into the organic oligomers, creating a surplus of π-electrons that populate previously unoccupied energy levels and bringing the whole system to completely different phases (28, 29).

Here, we demonstrate the realization of a text-book spin $S = 1/2$ Heisenberg chain (Fig. 1) (30, 31), within metal-free organic chains through a strategic on-surface synthesis of nitrogen doped chains derived from an aza-coronene building block. We synthesized a unit of the diazahexabenzocoronene (N$_2$HBC) molecule (32) and N$_2$HBC chains that present a perfect alignment of spin $S = 1/2$ units represented by the simple Heisenberg Hamiltonian with exchange coupling J between neighboring units

$$\hat{H} = \sum_i J\vec{S}_i \cdot \vec{S}_{i+1} \tag{1}$$

where $\vec{S}_i$ denotes the spin half operator at site i. We were able to theoretically and experimentally establish the behavior of the Heisenberg chains and correlate the number of units that each chain is formed (even or odd) with their collective quantum spin excitations in low-bias scanning tunneling spectroscopy (STS) experiments. These molecular chains offer a flexible platform for the design and experimental realization of spin lattices.

RESULTS

On-surface synthesis of N$_2$HBC molecule and respective chains

The precursor molecule **1** was prepared according to the same procedure as in the literature (see the Supplementary Materials for the details) (33). The corresponding reaction processes were shown in Fig. 1. Annealing the precursor molecules on Au(111) at 300°C led to the formation of the hexagonal monomer (dashed circles in Fig. 2A) and its oligomers with different lengths (yellow arrows in Fig. 2A), as well as nanoribbons (blue arrows in Fig. 2A). The synthesis of the nanoribbons indicates that the precursor molecule was initially split (molecule **2**) and subsequently connected to each other (see the

[1]International Center for Young Scientists, National Institute for Materials Science, 1-2-1 Sengen, Tsukuba, Ibaraki 305-0047, Japan. [2]Center for Basic Research on Materials, National Institute for Materials Sciences, 1-2-1 Sengen, Tsukuba, Ibaraki 305-0047, Japan. [3]Department of Applied Physics, Aalto University, Espoo, Finland. [4]School of Chemistry, Chemical Engineering and Biotechnology, Nanyang Technological University, 21 Nanyang Link, Singapore 637371, Singapore. [5]WPI Nano Life Science Institute (WPI-NanoLSI), Kanazawa University, Kakuma-machi, Japan. [6]Graduate School of Pure and Applied Sciences, University of Tsukuba, Tsukuba, 305-8571, Japan.
*Corresponding author. Email: kawai.Shigeki@nims.go.jp (S.K.); adam.foster@aalto.fi (A.S.F.); sgito@ntu.edu.sg (S.I.)
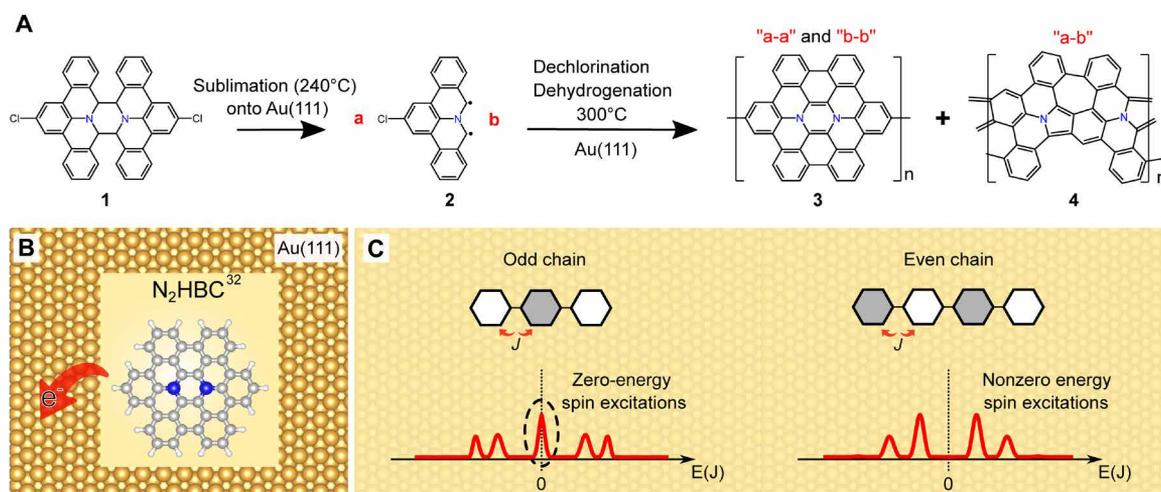
Fig. 1. Scheme of the reaction processes and resulting structures. (**A**) Reaction processes to form an $S = 1/2$ unit and the oligomers (N_2HBC chains) as well as graphene nanoribbon. (**B**) N_2HBC single molecule donates one electron to the surface, achieving an $S = 1/2$ spin state. (**C**) Schematic drawing of Heisenberg $S = 1/2$ antiferromagnetic molecular chains composed of odd and even numbers of molecular units and the corresponding magnetic couplings.
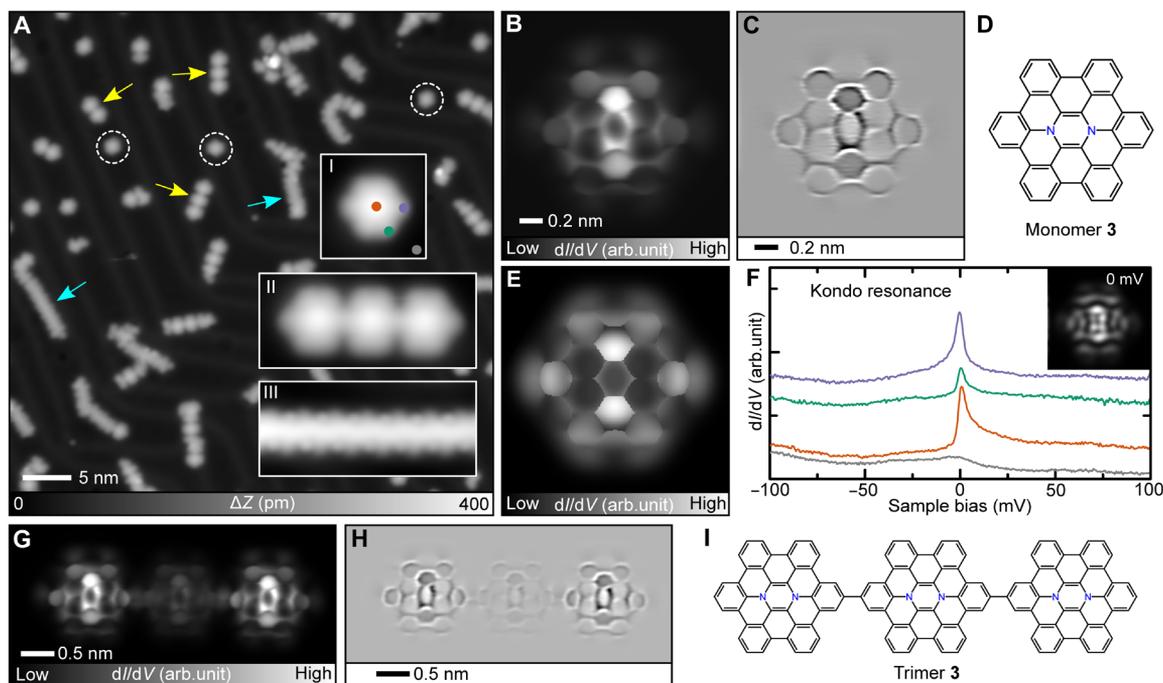

Fig. 2. Synthesis of N_2HBC molecule and respective chains 3. (**A**) STM topography of a Au(111) surface after annealing at 300°C for 5 min. Insets I, II, and III show close-up views of three different products. (**B**) Constant height dI/dV map of individual **3** and (**C**) the corresponding Laplace filtered image and (**D**) the chemical structure. (**E**) The simulation of constant height dI/dV map is performed using a relaxed CO tip. Constant height dI/dV simulations were acquired with a mixture of s and p_{xy} wave tips considering different ratios. The comparison of simulated images with different tips is presented in note S1 and figs. S6 and S7. (**F**) dI/dV curves recorded at three different sites on the molecule and one site on Au(111) as a reference, as indicated by colored dots in the left inset. The right inset shows the spatial distribution of the Kondo resonance state. (**G** to **I**) Constant height dI/dV map of individual trimer-N_2HBC^{3+} (G) and the corresponding Laplace filtered image (H) and the chemical structure (I). Measurement parameters: Sample bias voltage $V = 200$ mV and tunneling current $I = 5$ pA in (A). $V = 200$ mV and $I = 5$ pA in inset I of (A), $V = 200$ mV and $I = 3$ pA in inset II of (A), and $V = 200$ mV and $I = 10$ pA in inset III of (A). $V = 1$ mV and $V_{ac} = 10$ mV in (B) and (G).

Supplementary Materials, inset III of Fig. 2A and figs. S1 to S4). The complicated reaction pathways and the presence of coexisting nanoribbons limited the length the oligomer with the hexagonal unit up to heptamer (fig. S5). Since we are interested in the exploration of possible molecular spin structures, we focus on the hexagonal monomer and its oligomers and do not discuss the nanoribbons further.

To investigate the chemical structures of the products, the scanning tunneling microscopy (STM) tip apex was terminated with a carbon monoxide (CO) molecule (*34*, *35*). Inset I of Fig. 2A shows the close-up view of the monomer, whose inner structure was clearly observed in the constant height dI/dV map (Fig. 2B) and the corresponding Laplace filtered image (Fig. 2C). We found that the synthesis of the

N2HBC molecule (Fig. 2D) resulted from the C—C recoupling, dechlorination, and dehydrogenation of two **2**. The constant height dI/dV map taken near the Fermi level has a higher intensity at the center, suggesting that the net spin arises from a pair of N atoms in the monomer. Density functional theory (DFT) calculations indicate that the gas-phase N2HBC molecule is in a closed-shell singlet state in its neutral form but assumes a cationic state when deposited on Au(111) due to misalignment of their Fermi levels, thus bringing the system to the open-shell $S = 1/2$ state. It was found that each N2HBC unit approximately donates one electron until the Fermi level of the chains matches that of the underlying substrate (see the work function calculations in table S1). A simulated constant-height dI/dV map of the positively charged N2HBC$^+$ at 0 mV (Fig. 2E) captures all the main features of the experiment. Therefore, the central high-intensity signal is attributed to the Kondo resonance, which can be seen in the low bias dI/dV spectrum (Fig. 2F). Inset II in Fig. 2A was a trimer-N2HBC^{3+}, in which each unit is connected by a C—C bond (Fig. 2, G and H). Such coordinated fusion leads to the structure seen in Fig. 2I having all nitrogen atoms along the longitudinal direction of the chain. The unit in the center of the trimer-N2HBC^{3+} chain shows a darker contrast than the other peripheral two units in the dI/dV map (Fig. 2G).

Electronic structure characterization of the N2HBC chains

We conducted STS measurements over a pentamer of N2HBC (inset of Fig. 3A) and performed DFT and mean-field (MF)–Hubbard calculations of a periodic chain made of N2HBC$^+$ units. The dI/dV spectra, along with that on a bare Au(111) substrate (gray curve) as a reference, exhibits several characteristic peaks (Fig. 3A). We identified −0.7 V as the singly occupied molecular orbital (SOMO in Fig. 3B) and 0.5 V as the singly unoccupied molecular orbital (SUMO in Fig. 3C), leading to an SOMO-SUMO gap of 1.2 eV (see fig. S8 for the electronic properties of the pentamer). The electronic properties of the N2HBC molecule and chains from dimer to tetramer were also measured by STS (figs. S9 to S12), exhibiting similar SOMO-SUMO gaps and unoccupied states as compared to penta-N2HBC^{5+}. Substantial spectroscopic signatures observed around the Fermi level as indicated by the dashed rectangle in Fig. 3A suggest the presence of low-energy spin excitations in the penta-N2HBC^{5+}. Both DFT and MF-Hubbard calculations of free-standing periodic chain consisting of dimer-N2HBC^{2+} in its unit-cell indicate that its ground state is antiferromagnetic. MF-Hubbard calculations with $U = 1.5t$ (t is the nearest neighbors hopping parameter, we use $t = 2.7$ eV) leads to the total energy difference between antiferromagnetic and ferromagnetic states of about 10 meV. This value depends on U,
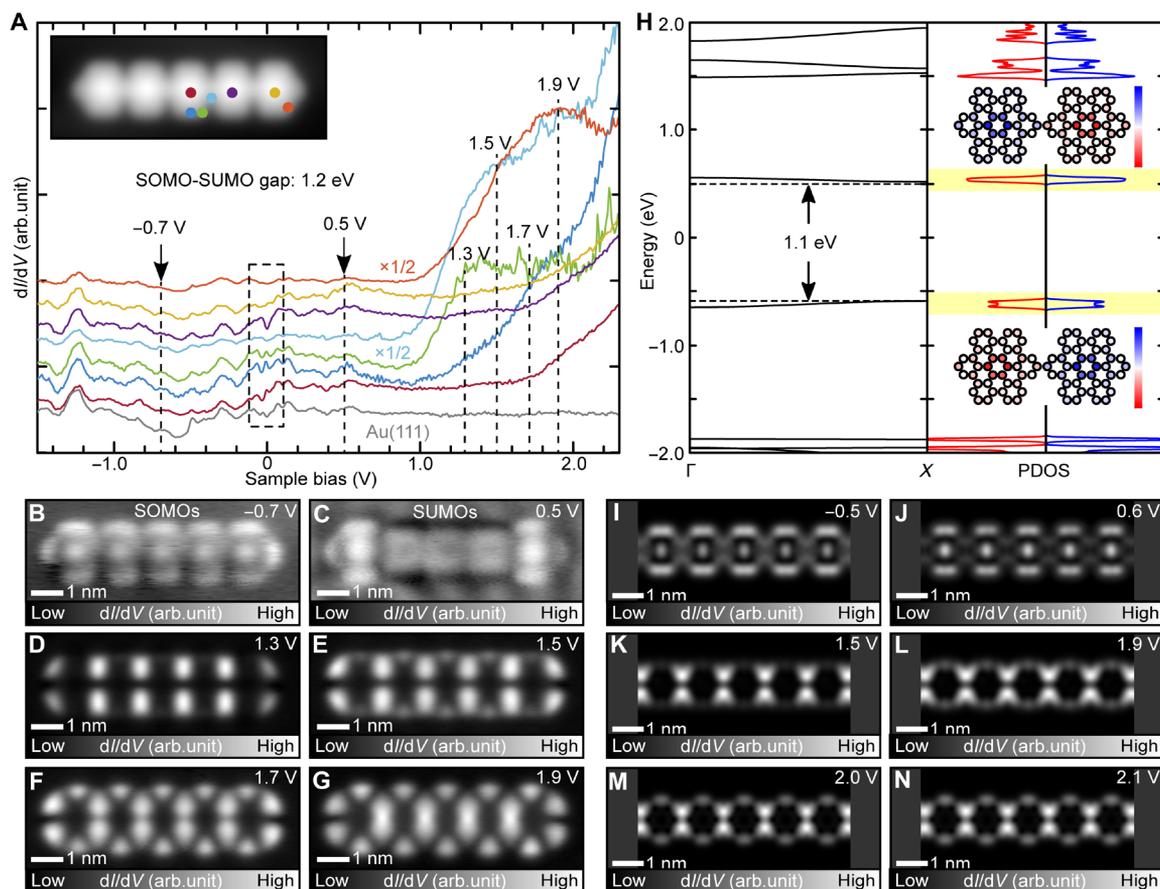

Fig. 3. Electronic properties of pentamer-N2HBC^{5+} 3. (A) dI/dV curves collected at different sites of the pentamer-N2HBC^{5+}, as indicated by colored dots in its STM topography (inset). **(B to G)** Constant current dI/dV maps measured at sample bias voltages of −0.7, 0.5, 1.3, 1.5, 1.7, and 1.9 V, respectively. **(H)** Band structure and spin polarized density of states (DOS) of a periodic antiferromagnetic chain. The inset shows the DOS map of the valence band (bottom) and conduction band (top) resolved by spin. **(I to N)** Constant height dI/dV maps were calculated at bias voltages corresponding to the simulated DOS. The simulations were carried out with a flexible CO tip (a combination of 13% of s and 87% of p_{xy} waves), which is comparable to the experimental ones. Measurement parameters: $V = −700$ mV, $I = 160$ pA, and $V_{ac} = 10$ mV in (B). For STS measurement, the tip-sample distance was adjusted at the corresponding bias voltages and $I = 160$ pA and $V_{ac} = 10$ mV in (C) to (G). PDOS, projected density of states.

reaching up to 21 meV for $U = 2.0t$. Following the same trend, DFT-B3LYP total energies indicate that the antiferromagnetic periodic chain is 97 meV more stable than its ferromagnetic counterpart. The stability of the chains through their total energies can be used to estimate the exchange coupling J, since the spin excitations will bring the periodic chains to a ferromagnetic excited state from an antiferromagnetic ground state. The fact that the DFT-B3LYP and MF-Hubbard modeling predict antiferromagnetic coupling between the units of the dimer-N_2HBC^{2+} chains in the absence of a substrate suggests that the role of any Ruderman-Kittel-Kasuya-Yosida (RKKY) interaction mediated by the metallic surface is negligible. The magnitude and nature of the coupling within the chains are more characteristic of the superexchange interaction seen in previous molecular systems (36–38). In the next section, we will discuss in more detail the comparison with the experimental data.

Figure 3H shows the DFT-B3LYP band structures and density of states (DOS) of the dimer-N_2HBC^{2+} periodic chain, revealing a bandgap of 1.1 eV, very close to the measured SOMO-SUMO gap of 1.2 eV (also see note S2 and figs. S13 to S15). The calculated local DOS maps obtained for the valence and conductance bands (see insets in Fig. 3H) highlight the antiferromagnetic behavior of the dimer-N_2HBC^{2+} chain: Both valence and conduction bands have alternating spin contributions in the central hexagon of the subsequent N_2HBC^+ units. Figure 3 (D to G) shows the constant current dI/dV maps at corresponding sample bias demonstrating the evolution of spatial distribution for these unoccupied states, and the same trend of the inner N_2HBC^+ units is observed in the simulated dI/dV maps in Fig. 3 (I to N). We note here that in the comparison between experimental (Fig. 3, B to G) and simulated maps (Fig. 3, I to N), the simulations are periodic and do not demonstrate the chain end effects seen in experiments.

Low-bias measurements and an effective model for N_2HBC chains

Next, we investigated the magnetic properties of the N_2HBC^+ chains up to maximum observed experimentally, the heptamer, by low-bias constant height STS measurements around the Fermi level, in which we collected dI/dV curves on the N_2HBC^+ units of each chain and dI/dV maps on selected bias values (Fig. 4). Local spin excitations that influence the inelastic tunneling spectroscopy of each chain were treated by the dynamical spin correlator (DSC) $A(\omega, n)$

$$A(\omega, n) = \langle GS | S_n^- \delta\left(\omega + E_{GS} - \hat{H}\right) S_n^+ | GS \rangle \quad (2)$$

which takes the many-body ground state $|GS\rangle$ and energies E_{GS} obtained by solving Eq. 1 (39–41). The frequency of the excitation ω corresponds to the applied bias voltage in the experiment, n indicates which unit is treated within the chain and $S_n^\pm = S_n^x \pm iS_n^y$. As the spin spectral weight of the magnetic units is related to the dI/dV line shape (42) and consequently its spatial distribution, we coupled the DSC to both DFT dI/dV simulated maps and MF-Hubbard spin densities by modulating their spatial distribution with $A(\omega, n)$, allowing us to emulate the conduction maps and establish their behavior with the size and parity of the chains and to their spin polarization.

We observed a systematic behavior of the dI/dV curves and the DSC relative to the number of N_2HBC^+ units, in which we assigned as even (Fig. 4, A to H, and fig. S16) or odd (Fig. 4, I to T, and fig. S17) Heisenberg chains according to their parity. For the dimer-N_2HBC^{2+}

in Fig. 4A, there is no prominent Kondo peak at the Fermi level, and we find symmetric conduction peaks around the Fermi level in the dI/dV curves acquired above each unit of the dimer. The constant height dI/dV map of dimer-N_2HBC^{2+} collected at 1 mV reveals that the signal is quite uniform over all the structure (fig. S18) while still resembling the signal from a single N_2HBC^+ molecule at 0 V. The tunneling conduction peaks of the dimer-N_2HBC^{2+} are consistent with the peaks of the DSC calculated with $J = 30$ meV (Fig. 4B), in agreement with the experimental value (fig. S16) and within the range of our MF-Hubbard estimated exchange coupling (between 20 and 40 mV) and DFT (see the Supplementary Materials for more details of the calculations, note S3, and figs. S14, S15, and S19 to 21). The two spin-1/2 subunits in the dimer are antiferromagnetically coupled, and the low-energy spectroscopic features correspond to an inelastic singlet-triplet excitation ($S = 0$ to $S = 1$). Both N_2HBC^+ units display equal intensity as simulated in the energy-normalized conductance maps, and both DFT and MF-Hubbard spin densities are concentrated over the central part of each molecule-unit where the N pair is located (fig. S18). The same behavior as for the dimer is observed in the dI/dV curves of the tetramer-N_2HBC^{4+} (Fig. 4E), with no prominent Kondo peak and symmetric conduction peaks around the Fermi level, and the assignment of the phenomenology is similar. No strong feature is observed at 0 V in the dI/dV curves, and the dI/dV map taken at 1 mV has a slightly brighter signal at the peripheral N_2HBC^+ units (fig. S18). We then extended our dimer-N_2HBC^{2+} model to a four spin-1/2 system in the tetramer-N_2HBC^{4+}, keeping the same exchange coupling $J = 30$ mV. The DSC gives several peaks around the Fermi level, consistent with the conduction peaks in the dI/dV curves (Fig. 4H). Unexpectedly, the DSC-modulated conductance map simulations in (fig. S18) correctly display the slightly stronger intensity over both peripheral units in the tetramer-N_2HBC^{4+} as observed in the experimental map. The MF-Hubbard spin density of the tetramer-N_2HBC^{4+} shows that the spin distributes at center of each unit, similar to the one obtained for the dimer-N_2HBC^{2+} (fig. S18). Constant height conduction maps for both dimer and tetramer at higher energies display comparable spin intensity with the simulated ones (Fig. 4, C, D, G, and H), which also correlate to DSC-modulated simulations. The hexamer also exhibits similar dI/dV curves to those of the tetramer (fig. S16) although the excitation gap is smaller. To investigate the relationship between chain length and spin excitation energy, d^2I/dV^2 spectra were measured on the chains with different lengths. We found that the lowest spin excitation energies of the dimer, tetramer, and hexamer were 30, 14, and 6 meV, respectively (fig. S16), generally consistent with the calculated values of 30, 19, and 14 meV. As the chain length increases, the energy values decrease (Fig. 4U). However, the number of the units was not large enough to demonstrate gapless spinon excitations.

The spectroscopy features of the odd Heisenberg chains (Fig. 4, I and O, and fig. S17) seem to contrast to the features observed in the even cases, as several peaks with different intensities and broadenings are observed in the tunneling conductance curves at the Fermi level. However, we demonstrate that they are still characteristic of a chain with only exchange coupling between spin-1/2 N_2HBC^+ units. In Fig. 4 (I and O), the dI/dV curves of both trimer-N_2HBC^{3+} and pentamer-N_2HBC^{5+} chains reveal zero-bias resonance peaks at the peripheral N_2HBC^+ units, with extra symmetric peaks in the dI/dV curves at higher bias voltages. While the dI/dV curves taken at the central N_2HBC^+ unit of the trimer-N_2HBC^{3+}
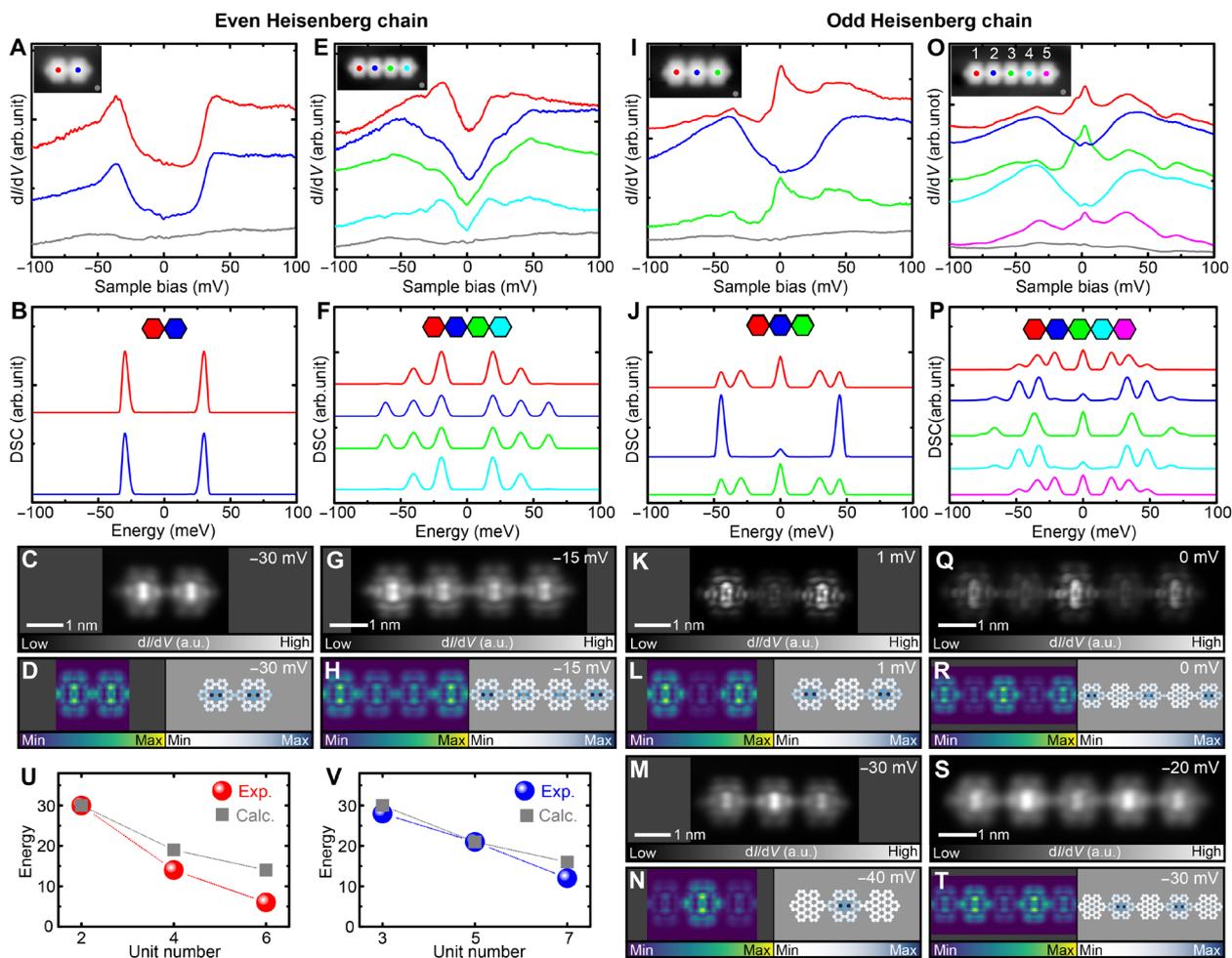
Fig. 4. Magnetic properties of even and odd Heisenberg chains on Au(111). Experimental dI/dV curves and constant height maps and simulations for dimer (**A** to **D**), tetramer (**E** to **H**), trimer (**I** to **N**), and pentamer (**O** to **T**). The insets in (A), (E), (I), and (O) correspond to the STM topography of each chain, with the colored dots indicating the STS measurement positions [gray color is the signal from the Au(111) substrate for reference]. The colored hexagons in (B), (F), (J), and (P) indicate in which unit of the chains the DSC was projected. The simulated DSC of spin excitations for chains, where we adopted a small broadening factor ($\delta = 5$), allows a better identification of the spin excitations (fig. S26). [(D), (H), (L), (N), (R), and (T)] Simulations were obtained by modulating the DFT calculated constant-height dI/dV maps at 0 meV with the DSC at respective energies in the left and were acquired by modulating the spin densities calculated by MF-Hubbard with the DSC in the right panel. (**U** and **V**) The relationship between the lowest spin excitation energy and the chain length summarized from the STS measurement and calculations. Measurement parameters: $V = -30$ mV and $V_{ac} = 3$ mV in (C) and (M). $V = -15$ mV and $V_{ac} = 2$ mV in (G). $V = -20$ mV and $V_{ac} = 2$ mV in (S). $V = 1$ mV and $V_{ac} = 10$ mV in (K). $V = 0$ mV and $V_{ac} = 1$ mV in (Q). a.u., arbitrary units.

are apparently featureless at the Fermi level (Fig. 4I), the central N$_2$HBC$^+$ unit in the pentamer-N$_2$HBC^{5+} has the same zero-bias features as the peripheral ones, with stronger intensity (Fig. 4O). In contrast, the N$_2$HBC$^+$ units next to the central one have no features at the Fermi level (see more details in the two-dimensional dI/dV map composed of 121 dI/dV curves taken along the pentamer-N$_2$HBC^{5+} chain in fig. S22). The relative contrast of the molecular units inverts at higher bias—this is particularly visible in the dI/dV maps: The constant height dI/dV maps of the trimer-N$_2$HBC^{3+} taken at 1 mV (Fig. 4K) corroborate to the strong intensity of the zero-bias peak at the peripheral N$_2$HBC$^+$ units, while at −30 mV, (Fig. 4M) the signal from the central N$_2$HBC$^+$ unit becomes more intense relative to the peripheral units. The DSC calculated at the peripheral units of the trimer-N$_2$HBC^{3+} (Fig. 4J) reveals a sharp peak at the Fermi level, consistent with the zero-bias resonances observed in the experiment, which is attributed to an emergent

collective twofold degenerate ground state that is only possible due to the odd number of spin-1/2 units, allowing the development of a Kondo resonance when in contact with the conduction electrons in the substrate. For higher energies, other steps consistent with higher-order inelastic spin excitations are also observed. On the other hand, the DSC calculated at the central unit of the trimer-N$_2$HBC^{3+} reveals a quenched zero-bias peak and a single sharp peak for higher and lower energies. Given the simplicity of the trimer-N$_2$HBC^{3+} case, we were able to describe in more detail the zero-bias spin excitations by analytically solving the Hamiltonian in Eq. 1. The twofold degenerate many-body states that result in $S^z = \pm 1/2$ are $|\alpha\rangle = \frac{1}{\sqrt{6}}(|\uparrow\uparrow\downarrow\rangle - 2|\uparrow\downarrow\uparrow\rangle + |\downarrow\uparrow\uparrow\rangle)$ and $|\beta\rangle = \frac{1}{\sqrt{6}}(|\downarrow\downarrow\uparrow\rangle - 2|\downarrow\uparrow\downarrow\rangle + |\uparrow\downarrow\downarrow\rangle)$ (see note S4 for the details). Note that the units at the edges of the chain are equivalent as given by mirror symmetry, whereas the central unit is different. This stems

from the open boundary conditions of the chain. At zero frequency (or zero bias), the DSC is proportional to the $\langle \alpha | S_n^+ | \beta \rangle^2$ matrix element of the ladder operator (*42*) that will flip a single spin in the unit *n* of the trimer where the excitation occurs. The matrix element calculated flipping the spin in the peripheral units is four times larger than the one calculated at the central unit, giving rise to more intense zero-bias peak as seen in the DSC curve Fig 4J (see the Supplementary Materials for a short summary of the calculation). The DSC-modulated conductance map shown in Fig. 4L correctly displays the contrast obtained in the experiment, demonstrating that the zero-bias contrast is related to the development of a Kondo resonance when in contact with the conduction electrons in the substrate. The inverted behavior of the tunneling conductance at −30 mV is also captured in the simulated maps, which agrees well with the experimental one, shown in Fig. 4 (M and N).

Extending our analysis from the trimer-N_2HBC^{3+} to the pentamer-N_2HBC^{5+} becomes then straightforward with our model, reproducing especially all the zero-bias resonances and their respective intensities [see Fig. 4 (O to T)], which are also related to elastic spin excitations and some inelastic excitations. To verify our experimental and theoretical findings, the heptamer was also investigated by STS measurements (fig. S17). We found the similar electronic behavior as the zero-energy peaks exist only in units with an odd number, while units with an even number primarily exhibit extra symmetric peaks. Furthermore, the d^2I/dV^2 spectra revealed that the lowest spin excitation energies for the trimer, pentamer, and heptamer are 29, 21, and 12 meV, respectively (fig. S17), in good agreement with the theoretical calculations of 30, 21, and 16 meV. The energy exhibits a decreasing trend with increasing chain length (Fig. 4V). Figure S23 shows a schematic visualization of the DSC calculated at several different energies from 1 to 45 meV, depicting the expected relative behavior of the contrasts in each unit for all chains. Together with that, it also shows that scaling from the numbers of molecules will allow us to explore the development of 1/2 Heisenberg spin structure according to the number of molecular components and the transition from expected Kondo resonances for odd chains to quenching in longer chains. The fine tuning of the spin excitation, together with the full control of the number of molecules, is a key step to engineering of spin coherence times and realizable spintronics.

Additional supporting measurements using an $AuSi_x$ intercalation layer between the N_2HBC chains and the Au(111) substrate are shown in the Supplementary Materials (note S5 and fig. S24). The spin excitation energy for the dimer on $AuSi_x$/Au(111) is larger than that on Au(111). This is due to the decoupling effect of the $AuSi_x$ layer, which reduces the polarization effect of the substrate, thereby increasing the excitation energy value (*43*, *44*). Furthermore, even when located on the $AuSi_x$ layer, the dimers can exhibit different values of spin excitation energy (fig. S25). This variation in excitation energy may result from the differing adsorption sites of the dimers on the $AuSi_x$ surface.

DISCUSSION
We successfully fabricated spin-1/2 Heisenberg chains with a single antiferromagnetic coupling *J* by covalently connecting diazahexabenzocoronene molecules. These molecular spin chains depict different collective features depending on their parity of the chains: gapped excitations for an even number of repeating units and Kondo

excitations for those with an odd number. A combination of STM/STS experiments and DFT simulations were used to fully determine their chemical structures, as well as their electronic and magnetic properties, and the complex excitations observed in the low-energy spectra were correctly addressed by the spin-1/2 Heisenberg Hamiltonian with a single antiferromagnetic coupling between first neighbors. Our results show that the experimental construction of molecular spin units provides a feasible way to realize the quantum Heisenberg spin-1/2 model, allowing direct imaging of the spatial distribution of its quantum many-body excitations. In particular, a molecular system with antiferromagnetic Heisenberg couplings presents a platform for the realization of topological spin models with fractionalized excitations (e.g., dimer chains and lattices) and frustrated spin systems.

MATERIALS AND METHODS
STM experiments
All experiments were performed in a low-temperature STM system (home-made) at 4.3 K under ultrahigh vacuum condition ($<2 \times 10^{-10}$ mbar). A clean single crystal Au(111) substrate was prepared through cyclic sputtering (Ar^+, 10 min) and annealing (720 K, 15 min). The temperature of sample was measured by a thermocouple and a pyrometer. 2,13-Dichloro-7b,7c,18b,18c-tetrahydro-$3a^2$,$7c^1$-diazahexabenzo[*a,cd,f,j,lm,o*]perylene (**1**) was deposited from Knudsen cells (Kentax GmbH). A STM tip was made from the chemically etched tungsten. For constant height d*I*/d*V* imaging, the tip apex was functionalized by a CO molecule picked up from the surface. The bias voltage was set close to zero voltage. The modulation amplitude was 10 mV_{0-peak}, and the frequency was 510 Hz for the wide energy range STS measurements and bond resolved imaging. The modulation amplitude ranged from 1 to 5 mV_{0-peak}, and the frequency was 510 Hz for the small energy range STS measurements.

Synthesis of compound 1
A solution of 2-chloro-8*H*-isoquinolino[4,3,2-*de*]phenanthridin-9-ium chloride (10 mg, 0.030 mmol) dissolved in dimethylsulfoxide (2.0 ml) was preheated to 190°C for 30 s. Subsequently, tributylamine (0.17 ml, 0.71 mmol) was added and further stirred for 5 min. After cooling down to room temperature, the reaction mixture was extracted with dichloromethane. The combined organic phases were washed with water, dried under sodium sulfate, filtered, and evaporated in vacuo. The crude product was purified by silica gel column chromatography (hexane/dichloromethane = 8/1) to afford 2,13-dichloro-7b,7c,18b,18c-tetrahydro-$3a^2$,$7c^1$-diazahexabenzo[*a,cd,f,j,lm,o*]perylene (**1**) as a yellow solid (1.3 mg, 0.002 mmol, 7%). (See the Supplementary Materials for the details).

Theoretical calculations
Spin-polarized DFT calculations were performed using the FHI-AIMS code (*45*). Geometry optimizations were carried out twice, using two different exchange-correlation functionals: initial optimization with PBE (*46*) and then followed by B3LYP (*47*), both with the standard "light" basis set. For the gas phase modeled monomer, dimer, trimer, and the infinite chain, structural relaxations were only allowed in *xy* plane (see the comparison of constrained and unconstrained relaxations in fig. S19). For all the d*I*/d*V* simulations of monomer, the adsorption of monomer was first modeled on Au(111) with three atomic layers, and two bottom layers were fully

constrained. All free atoms were allowed to relax until the residual atomic forces reached less than $5e^{-3}$ eV/Å. For the periodic chain, we used a distance of 15 Å to avoid interactions between the nonperiodic images, and the geometry was relaxed using only the Γ-point. We used eight times denser k-grid in the periodic direction to calculate band structures and DOSs. The MF-Hubbard calculations were realized with the PYQULA library (48), while the DSCs were calculated using the DMRGPY library (41).

Theoretical constant height dI/dV maps were simulated using either fixed or relaxed CO tips, as specified in the relevant text. Simulations with fixed tips were computed by means of PPSTM code (49), using a mixture of s and p_{xy} waves—different ratios of these waves were considered (see the Supplementary Materials) (50, 51). For the simulations using relaxed tips, the PPAFM code was initially used to model the positions of the CO tips (52). The lateral stiffness for the CO tip was set to 0.25 N/m, and an oscillation amplitude of 1.0 Å was used. Subsequently, the dI/dV maps were generated by PPSTM with a mixed sp-wave tip in a ratio that best reproduces the experiments. We used a broadening parameter of 0.1 eV for all simulations to get a good simulation performance.

Supplementary Materials

This PDF file includes:
Synthesis of 1
Supplementary Notes S1 to S5
Figs. S1 to S26
Table S1
References

REFERENCES AND NOTES

1. J. Fernández-Rossier, J. J. Palacios, Magnetism in graphene nanoislands. *Phys. Rev. Lett.* **99**, 177204 (2007).

2. A. R. Rocha, V. M. García-suárez, S. W. Bailey, C. J. Lambert, J. Ferrer, S. Sanvitoet, Towards molecular spintronics. *Nat. Mater.* **4**, 335–339 (2005).

3. O. V. Yazyev, Emergence of magnetism in graphene materials and nanostructures. *Rep. Prog. Phys.* **73**, 056501 (2010).

4. D. Pesin, A. H. MacDonald, Spintronics and pseudospintronics in graphene and topological insulators. *Nat. Mater.* **11**, 409–416 (2012).

5. H. Min, J. E. Hill, N. A. Sinitsyn, B. R. Sahu, L. Kleinman, A. H. MacDonald, Intrinsic and Rashba spin-orbit interactions in graphene sheets. *Phys. Rev. B.* **74**, 165310 (2007).

6. O. V. Yazyev, M. I. Katsnelson, Magnetic correlations at graphene edges: Basis for novel spintronics devices. *Phys. Rev. Lett.* **100**, 047209 (2008).

7. N. Tombros, C. Jozsa, M. Popinciuc, H. T. Jonkman, B. J. van Wees, Electronic spin transport and spin precession in single graphene layers at room temperature. *Nature* **448**, 571–574 (2007).

8. O. V. Yazyev, Hyperfine interactions in graphene and related carbon nanostructures. *Nano Lett.* **8**, 1011–1015 (2008).

9. F. Lombardi, A. Lodi, J. Ma, J. Liu, M. Slota, A. Narita, W. Myers, K. Müllen, X. Feng, L. Bogani, Quantum units from the topological engineering of molecular graphenoids. *Science* **366**, 1107–1110 (2019).

10. L. Grill, S. Hecht, Covalent on-surface polymerization. *Nat. Chem.* **12**, 115–130 (2020).

11. L. Grill, M. Dyer, L. Lafferentz, M. Persson, M. V. Peters, S. Hecht, Nano-architectures by covalent assembly of molecular building blocks. *Nat. Nanotechnol.* **2**, 687–691 (2007).

12. D. G. de Oteyza, T. Frederiksen, Carbon-based nanostructures as a versatile platform for tunable π-magnetism. *J. Phys. Condens. Matter* **34**, 443001 (2022).

13. S. Mishra, D. Beyer, K. Eimre, S. Kezilebieke, R. Berger, O. Gröning, C. A. Pignedoli, K. Müllen, P. Liljeroth, P. Ruffieux, X. Feng, R. Fasel, Topological frustration induces unconventional magnetism in a nanographene. *Nat. Nanotechnol.* **15**, 22–28 (2020).

14. J. Li, S. Sanz, M. Corso, D. J. Choi, D. Peña, T. Frederiksen, J. I. Pascual, Single spin localization and manipulation in graphene open-shell nanostructures. *Nat. Commun.* **10**, 200 (2009).

15. S. Mishra, D. Beyer, K. Eimre, J. Liu, R. Berger, O. Gröning, C. A. Pignedoli, K. Müllen, R. Fasel, X. Feng, P. Ruffieux, Synthesis and characterization of π-extended triangulene. *J. Am. Chem. Soc.* **141**, 10621–10625 (2019).

16. J. Su, M. Telychko, P. Hu, G. Macam, P. Mutombo, H. Zhang, Y. Bao, F. Cheng, Z.-Q. Huang, Z. Qiu, S. J. R. Tan, H. Lin, P. Jelínek, F.-C. Chuang, J. Wu, J. Lu, Atomically precise bottom-up synthesis of π-extended [5]triangulene. *Sci. Adv.* **5**, eaav7717 (2019).

17. J. Li, S. Sanz, J. Castro-Esteban, M. Vilas-Varela, N. Friedrich, T. Frederiksen, D. Peña, J. I. Pascual, Uncovering the triplet ground state of triangular graphene nanoflakes engineered with atomic precision on a metal surface. *Phys. Rev. Lett.* **124**, 177201 (2020).

18. Y. Zheng, C. Li, C. Xu, D. Beyer, X. Yue, Y. Zhao, G. Wang, D. Guan, Y. Li, H. Zheng, J. Liu, X. Wang, W. Luo, X. Feng, S. Wang, J. Jia, Designer spin order in diradical nanographenes. *Nat. Commun.* **11**, 6076 (2020).

19. Q. Sun, X. Yao, O. Gröning, K. Eimre, C. A. Pignedoli, K. Müllen, A. Narita, R. Fasel, P. Ruffieux, Coupled spin states in armchair graphene nanoribbons with asymmetric zigzag edge extensions. *Nano Lett.* **20**, 6429–6436 (2020).

20. S. Mishra, X. Yao, Q. Chen, K. Eimre, O. Gröning, R. Ortiz, M. Di Giovannantonio, J. C. Sancho-García, J. Fernández-Rossier, C. A. Pignedoli, K. Müllen, P. Ruffieux, A. Narita, R. Fasel, Large magnetic exchange coupling in rhombus-shaped nanographenes with zigzag periphery. *Nat. Chem.* **13**, 581–586 (2021).

21. K. Sun, O. J. Silveira, S. Saito, K. Sagisaka, S. Yamaguchi, A. S. Foster, S. Kawai, Manipulation of spin polarization in boron-substituted graphene nanoribbons. *ACS Nano* **16**, 11244–11250 (2022).

22. X. Xu, K. Sun, A. Ishikawa, A. Narita, S. Kawai, Magnetism in nonplanar zigzag edge termini of graphene nanoribbons. *Angew. Chem. Int. Ed.* **62**, e202302534 (2023).

23. R. D. McCurdy, A. Delgado, J. Jiang, J. Zhu, E. C. H. Wen, R. E. Blackwell, G. C. Veber, S. Wang, S. G. Louie, F. R. Fischer, Engineering robust metallic zero-mode states in olympicene graphene nanoribbons. *J. Am. Chem. Soc.* **145**, 15162–15170 (2023).

24. C. Zhao, G. Catarina, L. Zhang, J. C. G. Henriques, L. Yang, J. Ma, X. Feng, O. Gröning, P. Ruffieux, J. Fernández-Rossier, R. Fasel, Tunable topological phases in nanographene-based spin-½ alternating-exchange Heisenberg chains. *Nat. Nanotechnol.* **19**, 1789–1795 (2024).

25. J. Hieulle, S. Castro, N. Friedrich, A. Vegliante, F. R. Lara, S. Sanz, D. Rey, M. Corso, T. Frederiksen, J. I. Pascual, D. Peña, On-surface synthesis and collective spin excitations of a triangulene-based nanostar. *Angew. Chem. Int. Ed.* **60**, 25224–25229 (2021).

26. S. Mishra, G. Catarina, F. Wu, R. Ortiz, D. Jacob, K. Eimre, J. Ma, C. A. Pignedoli, X. Feng, P. Ruffieux, J. Fernández-Rossier, R. Fasel, Observation of fractional edge excitations in nanographene spin chains. *Nature* **598**, 287–292 (2021).

27. Y. Zhao, K. Jiang, C. Li, Y. Liu, G. Zhu, M. Pizzochero, E. Kaxiras, D. Guan, Y. Li, H. Zheng, C. Liu, J. Jia, M. Qin, X. Zhuang, S. Wang, Quantum nanomagnets in on-surface metal-free porphyrin chains. *Nat. Chem.* **15**, 53–60 (2023).

28. E. C. Ho Wen, P. H. Jacobse, J. Jiang, Z. Wang, R. D. McCurdy, S. G. Louie, M. F. Crommie, R. Fischer, Magnetic interactions in substitutional core-doped graphene nanoribbons. *J. Am. Chem. Soc.* **144**, 13696–13703 (2022).

29. E. C. H. Wen, P. H. Jacobse, J. Jiang, Z. Wang, S. G. Louie, M. F. Crommie, F. R. Fischer, Fermi-level engineering of nitrogen core-doped armchair graphene nanoribbons. *J. Am. Chem. Soc.* **145**, 19338–19346 (2023).

30. H. Z. Bethe, Zur Theorie der Metalle. *Zeitschrift für Physik* **71**, 205–226 (1931).

31. S. Murmann, F. Deuretzbacher, G. Zürn, J. Bjerlin, S. M. Reimann, L. Santos, T. Lompe, S. Jochim, Antiferromagnetic Heisenberg spin chain of few cold atoms in a one-dimensional trap. *Phys. Rev. Lett.* **115**, 215301 (2015).

32. X.-Y. Wang, M. Richter, Y. He, J. Björk, A. Riss, R. Rajesh, M. Garnica, F. Hennersdorf, J. J. Weigand, A. Narita, R. Berger, X. Feng, W. Auwärter, J. V. Barth, C.-A. Palma, K. Müllen, Exploration of pyrazine-embedded antiaromatic polycyclic hydrocarbons generated by solution and on-surface azomethine ylide homocoupling. *Nat. Commun.* **8**, 1948 (2017).

33. R. Berger, A. Giannakopoulos, P. Ravat, M. Wagner, D. Beljonne, X. Feng, K. Müllen, Synthesis of nitrogen-doped zigzag-edge peripheries: Dibenzo-9a-azaphenalene as repeating unit. *Angew. Chem. Int. Ed.* **53**, 10520–10524 (2014).

34. R. Temirov, S. Soubatch, O. Neucheva, A. C. Lassise, F. S. Tautz, A novel method achieving ultra-high geometrical resolution in scanning tunnelling microscopy. *New J. Phys.* **10**, 053012 (2008).

35. L. Gross, F. Mohn, N. Moll, P. Liljeroth, G. Meyer, The chemical structure of a molecule resolved by atomic force microscopy. *Science* **325**, 1110–1114 (2009).

36. X. Chen, Y.-S. Fu, S.-H. Ji, T. Zhang, P. Cheng, X.-C. Ma, X.-L. Zou, W.-H. Duan, J.-F. Jia, Q.-K. Xue, Probing superexchange interaction in molecular magnets by spin-flip spectroscopy and microscopy. *Phys. Rev. Lett.* **101**, 197208 (2008).

37. D. Jacob, J. Fernández-Rossier, Theory of intermolecular exchange in coupled spin- 1/2 nanographenes. *J. Phys. Rev. B* **106**, 205405 (2022).

38. Y. Saleem, T. Steenbock, E. R. J. Alhadi, W. Pasek, G. Bester, P. Potasz, Superexchange mechanism in coupled triangulenes forming spin-1 chains. *Nano Lett.* **24**, 7417–7423 (2024).

39. M. Fishman, E. Stoudenmire, ITensor Team. ITensor Library. GitHub, https://github.com/ITensor/ITensor.

40. M. Fishman, S. R. White, E. M. Stoudenmire, The ITensor software library for tensor network calculations. *SciPost Phys. Codebases* **4**, 10.21468/SciPostPhysCodeb.4 (2022).

41. DMRGpy Library, http://github.com/joselado/dmrgpy.

42. J. Fernández-Rossier, Theory of single-spin inelastic tunneling spectroscopy. *Phys. Rev. Lett.* **102**, 256802 (2009).

43. O. Deniz, C. Sánchez-Sánchez, T. Dumslaff, X. Feng, A. Narita, K. Müllen, N. Kharche, V. Meunier, R. Fasel, P. Ruffieux, Revealing the electronic structure of silicon intercalated armchair graphene nanoribbons by scanning tunneling spectroscopy. *Nano Lett.* **17**, 2197–2203 (2017).

44. K. Sun, S. Kawai, Strength of electronic decoupling of fullerene on an $AuSi_X$ layer formed on Au(111). *Phys. Chem. Chem. Phys.* **23**, 5455–5459 (2021).

45. V. Blum, R. Gehrke, F. Hanke, P. Havu, V. Havu, X. Ren, K. Reuter, M. Scheffler, Ab initio molecular simulations with numeric atom-centered orbitals. *Comput. Phys. Commun.* **180**, 2175–2196 (2009).

46. J. P. Perdew, K. Burke, M. Ernzerhof, Generalized gradient approximation made simple. *Phys. Rev. Lett.* **77**, 3865–3868 (1996).

47. A. D. Becke, Density-functional thermochemistry. III. The role of exact exchange. *J. Chem. Phys.* **98**, 5648–5652 (1993).

48. J. L. Lado, Pyqula, GitHub, https://github.com/joselado/pyqula.

49. P. Hapala, G. Kichin, C. Wagner, F. S. Tautz, R. Temirov, P. Jelínek, Mechanism of high-resolution STM/AFM imaging with functionalized tips. *Phys. Rev. B* **90**, 085421 (2014).

50. B. de la Torre, M. Švec, G. Foti, O. Krejčí, P. Hapala, A. Garcia-Lekue, T. Frederiksen, R. Zbořil, A. Arnau, H. Vázquez, P. Jelínek, Submolecular resolution by variation of the inelastic electron tunneling spectroscopy amplitude and its relation to the AFM/STM signal. *Phys. Rev. Lett.* **119**, 166001 (2017).

51. L. Gross, N. Moll, F. Mohn, A. Curioni, G. Meyer, F. Hanke, M. Persson, High-resolution molecular orbital imaging using a *p*-wave STM tip. *Phys. Rev. Lett.* **107**, 086101 (2011).

52. O. Krejčí, P. Hapala, M. Ondráček, P. Jelínek, Principles and simulations of high-resolution STM imaging with a flexible tip apex. *Phys. Rev. B* **95**, 045407 (2017).

53. W. C. Still, M. Kahn, A. Mitra, Rapid chromatographic technique for preparative separations with moderate resolution. *J. Org. Chem.* **43**, 2923–2925 (1978).

54. B. Yang, J. Yang, J. Zhang, Synthesis of axially chiral anilides enabled by a palladium/ming-phos-catalyzed desymmetric Sonogashira reaction. *Chin. J. Chem.* **40**, 317–322 (2021).

55. S.-U. Yoo, N. Siemer, M. Todorova, D. Marx, J. Neugebauer, Deciphering charge transfer and electronic polarization effects at gold nanocatalysts on reduced titania support. *J. Phys. Chem. C* **123**, 5495–5506 (2019).